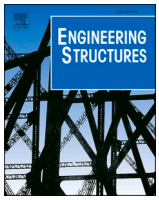
Engineering Structures 370 (2027) 124031



Contents lists available at ScienceDirect

Engineering Structures

journal homepage: www.elsevier.com/locate/engstruct



A Bayesian inference approach for probabilistic wind field retrieval of long-span bridges using coherent Doppler wind lidar

Longwen Fan [a], Yiming Zhang [a,*], Hao Wang [a,*], Jinlong Yuan [b], Xiao Pan [c], Shuo Zhang [b], Haiyun Xia [b]

[a] Key Laboratory of Concrete and Prestressed Concrete Structures of Ministry of Education, Southeast University, Nanjing, 211189, China
[b] State Key Laboratory of Climate System Prediction and Risk Management, Nanjing University of Information Science and Technology, Nanjing, 210044, China
[c] Department of Civil and Environmental Engineering, The Hong Kong University of Science and Technology, 999077, Hong Kong

ARTICLE INFO

Keywords:
Long-span bridge
Wind lidar
Probabilistic retrieval
Bayesian inference

ABSTRACT

Accurate characterization of full-scale wind fields provides important information for analysing the wind environment around long-span bridges. While coherent Doppler wind lidar (CDWL) provides advanced measurement methods, retrieving the complete vector wind field from a single-scan lidar is an ill-posed inverse problem. Traditional deterministic wind field retrieval methods can only provide a single estimate, failing to account for uncertainties caused by measurement noise, atmospheric turbulence, and geometric constraints. To address this limitation, this study proposes a Bayesian inference framework for probabilistic retrieval of the horizontal wind field around long-span bridges using CDWL. Specifically, this framework employs a prior distribution that integrates the background wind field and smoothness constraints, effectively mitigating the high-dimensional and ill-posed problem. The posterior distribution provides a mean estimate of the retrieved wind field, simultaneously quantifying the uncertainty of the retrieval process. Full-scale wind field measurements are conducted on the Ningyang Yangtze River Bridge. Multi-resolution CDWL data combined with on-site anemometer records provide support for evaluating retrieval accuracy and uncertainty characteristics. The proposed method is then compared with traditional Uniform Wind, Velocity Azimuth Process, Velocity Plan Processing, and Variational Method. The results show that the proposed method achieves the highest accuracy in retrieving horizontal wind fields around the bridge and provides the standard deviations of wind speed and direction. Furthermore, the anemometer measurements consistently fall within the retrieved confidence interval, highlighting the effectiveness of the method in quantifying wind field uncertainty.

1. Introduction

With the continuous growth of global transportation demands, an increasing number of long-span bridges are being constructed, particularly across wide rivers and coastal waterways [1,2]. These structures often feature slender and flexible design, making them highly susceptible to dynamic wind fields induced by atmospheric turbulence [3–5]. In addition, the complex terrain surrounding bridge sites further amplifies the spatial variability and non-uniformity of the local wind environment [6,7]. Wind load has become one of the critical factors influencing the design, construction, and long-term operation of long-span bridges [8–10].

A precise assessment of the wind loads acting on long-span bridges requires a comprehensive understanding of the surrounding dynamic and spatially evolving wind characteristics [11–13]. Traditionally, the aerodynamic behavior of bridges has been investigated through wind tunnel testing on scaled models and computational fluid dynamics simulations [14,15]. Although these methods provide valuable insights into bridge aerodynamics, they exhibit several inherent limitations. Both approaches typically rely on idealized inflow conditions, such as uniform and stationary flows perpendicular to the bridge axis, which do not accurately represent the highly non-uniform and non-stationary wind conditions in the real atmospheric boundary layer [16]. Moreover, discrepancies between the Reynolds numbers achievable in wind tunnel experiments or numerical simulations and those under full-scale conditions may lead to significant variations in wind–structure interactions across different scales [17]. Therefore, full-scale wind field measurements under realistic atmospheric conditions can validate and

* Corresponding authors.
E-mail addresses: yiming.zhang@seu.edu.cn (Y. Zhang), wanghao1980@seu.edu.cn (H. Wang).

https://doi.org/10.1016/j.engstruct.2026.124031
Received 18 May 2026; Received in revised form 2 September 2026; Accepted 23 October 2026
Available online 27 October 2026
0141-0296/© 2026 Elsevier Ltd. All rights are reserved, including those for text and data mining, AI training, and similar technologies.

refine existing design theories, thereby reducing the uncertainty in wind load assessment and enhancing the safety of bridge structures.

In-situ measurements using anemometers installed on the bridge decks and towers have historically served as the primary source of wind field data [18,19]. These point-based sensors provide wind information only at discrete locations and therefore cannot capture the continuous wind field structure across the entire bridge span and its surroundings environment [20]. Over the past decade, optical remote sensing technologies, such as scanning coherent Doppler wind lidar (CDWL), have developed rapidly [21,22]. CDWL eliminates the flow disturbances caused by traditional measurement towers or supporting masts [23] and enabling the collection of valuable wind data in areas inaccessible to personnel, including main girders over river surfaces and high-rise bridge towers [24–26]. However, a single scanning lidar can measure only the velocity component along the laser beam (radial velocity). Deriving the complete vector wind field from such measurements constitutes an ill-posed inverse problem that requires sophisticated retrieval algorithms [27–29].

Most conventional retrieval techniques are deterministic and provide only a single point estimate of the wind field [30,31]. These methods often fail to systematically account for and quantify the various sources of uncertainty, including instrumental noise, atmospheric turbulence fluctuations, and the inherent assumptions in the retrieval algorithms [32]. To overcome the limitations of deterministic point estimates, Bayesian inference offers a powerful probabilistic framework for wind field retrieval [33–35]. Bayesian methods treat the wind field parameters as random variables and infers their full posterior probability distribution by combining prior knowledge with the likelihood of the observations [36]. The resulting posterior distribution provides a mean estimate of the wind field and a rigorous quantification of its uncertainty. Nevertheless, applying Bayesian inference to retrieve the horizontal wind field around bridges based on CDWL observation data still faces three major obstacles [37,38]: (1) The prior distribution of the radar wind field typically incorporates only a single constraints, which may lead to unreliable estimates of the retrieved horizontal wind field; (2) Radial velocity measurements in regions with low carrier-to-noise ratio (CNR) may be insufficient for accurately retrieving the wind field; and (3) The retrieval problem is severely ill-posed and highly dimensional, typically involving thousands of unknown velocity vectors within a single scan. As a result, the strong turbulence and highly non-uniform wind environment around long-span bridges poses significant challenges for reliable wind field retrieval.

This study proposes a novel Bayesian inference framework that utilizes CDWL scan data to retrieve the two-dimensional (2D) horizontal wind field surrounding a long-span suspension bridge. The framework employs the prior distributions combining background flow information with smoothness constraints, effectively mitigating the high dimensionality and ill-posedness inherent in single-lidar wind field retrieval. Specifically, background priors act as weak constraints that provide valuable initial wind field estimates, whereas smoothness priors act as strong constraints that impose effective spatial smoothness. In addition, the framework quantifies retrieval uncertainty by deriving the posterior probability distribution from the observational data and the prior distributions. Full-scale wind field observations are conducted on the Ningyang Yangtze River Bridge. The effectiveness of the proposed method for wind field retrieval is validated by combining multi-resolution CDWL data with anemometer records at the bridge site. Compared with traditional deterministic approaches, the method yields more accurate wind field estimates and offers a rigorous quantification of retrieval uncertainty. Overall, this study presents a robust framework for wind field retrieval and uncertainty quantification around long-span bridges, contributing to the safe and reliable operation of these structures.

The rest of this paper is organized as follows. Section 2 details the Bayesian framework used for horizontal wind field retrieval. Section 3 provides an in-depth analysis of the horizontal wind field and uncertainty results retrieved from radar measurement data around the bridge. Finally, Section 4 summarizes the main findings and conclusions of this measurement study.

2. Methodology

2.1. Bayesian framework for wind field retrieval

To enhance the effectiveness and stability of wind field retrieval, a Bayesian framework is used to jointly model prior information with the lidar observation data, thereby achieving robust wind field estimation and quantifying its uncertainty [39,40].

The proposed Bayesian framework for probabilistic wind field retrieval is illustrated in Fig. 1, including the following three steps:

Step 1: Obtain raw observation data from the scanned CDWL. This step involves performing a Plane Position Indicator (PPI) scan over the entire span of the long-span bridge at low elevation angles. The radial speed field is obtained from the Doppler effect of the wind lidar echo signal. The observed radial speed and azimuth angle data are the primary inputs for Bayesian framework.
Step 2: Infer the posterior probability of the wind field based on these observational data. This process involves defining a prior probability distribution that incorporates background wind field and spatial smoothness, along with a likelihood function based on the statistical characteristics of observation errors. The Gibbs sampling algorithm is then used to efficiently solve high-dimensional problems of posterior probability distributions.
Step 3: Obtain the final retrieved wind field and its uncertainty from the posterior distribution. The mean of the posterior distributions is employed to retrieve the horizontal wind field, while the standard deviation of the samples is calculated to quantify the uncertainty of the retrieval process. Finally, the accuracy of the retrieval wind field is verified by comparing the results with in-situ anemometer measurements using multiple evaluation metrics.

2.2. Wind field retrieval from single lidar data

The fundamental problem of retrieving a wind field from lidar observations data can be summarized as follows: (1) using the partially known wind vector information, reasonable assumptions are made about the spatial distribution characteristics of the wind field. (2) constructing a parameterized wind field model in the target domain and applying analytical or numerical methods to retrieve the unknown components.

Specifically, the observed radial speed V_o and azimuth angle θ can be accurately obtained by the wind lidar with PPI scanning. The wind field is then retrieved by combining the tangential speed V_t. At low elevation angles, the radial speed and tangential speed can be expressed as

$$V_r = u\cos\theta + v\sin\theta \tag{1}$$

$$V_t = -u\sin\theta + v\cos\theta \tag{2}$$

where u and v are the two components of velocity in the lidar coordinate system xoy. V_r and V_t are the retrieved radial speed and tangential speed, respectively.

Differentiating Eq. (1) along the azimuth direction can be written as

$$\frac{\partial V_r}{\partial\theta} = -u\sin\theta + v\cos\theta + \frac{\partial u}{\partial\theta}\cos\theta + \frac{\partial v}{\partial\theta}\sin\theta \tag{3}$$

Combining Eqs. (2) and (3), we can obtain

$$V_t = \frac{\partial V_r}{\partial\theta} - \frac{\partial u}{\partial\theta}\cos\theta - \frac{\partial v}{\partial\theta}\sin\theta \tag{4}$$

To fully utilize the observed radial speed V_o, the two horizontal components obtained from the final Bayesian retrieval can be updated

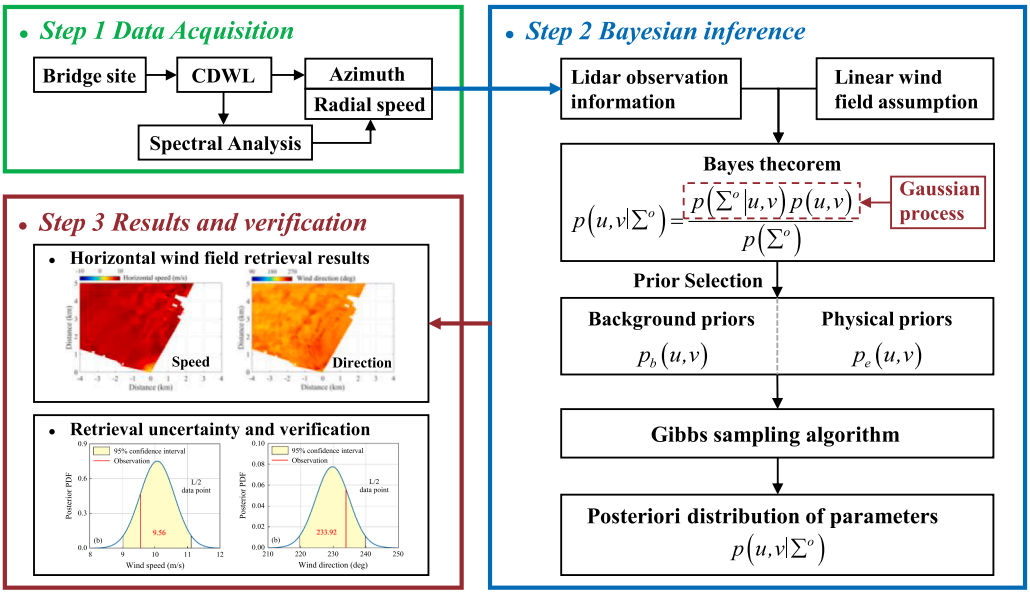


Fig. 1. The proposed Bayesian framework for wind field retrieval.

by

$$u = V_o \cos\theta - V_t \sin\theta \tag{5}$$

$$v = V_o \sin\theta + V_t \cos\theta \tag{6}$$

In the Bayesian retrieval framework, the horizontal wind field to be solved (including the u and v components at all grid points) is treated as a random variable, and the observed data (i.e., V_o and θ at all measurement points) are also treated as a random variable. The objective is to infer the probability distribution of the wind field conditioned on the observed data.

2.3. Bayesian inference for probabilistic retrieval

Bayesian inference treats parameters as random variables, with their uncertainty is represented by probability distributions [41]. These distributions describe the range of parameter values and their probabilities, enabling the evaluation of standard deviations and confidence intervals in the retrieval results. The Bayesian formulation can be expressed as

$$p\left(u,v\middle|\sum{}^{o}\right) = \frac{p(\sum{}^{o}|u,v)p(u,v)}{p(\sum{}^{o})} \tag{7}$$

where (u,v) is the horizontal wind field to be retrieved, $\sum^o$ is the observed data including V_o and θ, $p(u,v|\sum^o)$ is the posterior probability, $p(\sum^o|u,v)$ is the likelihood function, $p(u,v)$ is the prior probability, and $p(\sum^o)$ is the probability of the observation data $\sum^o$.

Once the $\sum^o$ have been observed, $p(\sum^o)$ is a constant and thus can be written as

$$p\left(u,v\middle|\sum{}^{o}\right) \propto p\left(\sum{}^{o}|u,v\right)p(u,v) \tag{8}$$

Since the normalization constant $p(\sum^o)$ cannot be calculated analytically, a Markov chain Monte Carlo method can be used to iteratively sample from the posterior distribution.

2.3.1. Prior Probability

The prior probability $p(u,v)$ is an informative prior that constrains the local solution, ensuring that the retrieved wind field is consistent and meteorologically plausible. In the present framework, two complementary sources of prior information are considered: a background wind-field prior and a spatial smoothness prior. The combined prior is defined as the normalized product of these two terms:

$$p(u,v) = \frac{1}{Z_p} p_b(u,v)\cdot p_e(u,v) \propto p_b(u,v)\cdot p_e(u,v) \tag{9}$$

where Z_p is the normalization constant. In the MCMC sampling procedure, this constant does not depend on (u, v) and therefore cancels out in the posterior proportionality.

Gaussian processes offer a flexible class of models [42], particularly for variables that exhibit spatial dependence. Assuming that the background wind field follows a multivariate normal distribution, its prior probability can be expressed as

$$p_b(u,v) = \frac{1}{(2\pi)^N |\boldsymbol{C}_b|^{1/2}} \exp\left(-\frac{1}{2}(\boldsymbol{m}-\boldsymbol{m}_b)^{\mathrm{T}} \boldsymbol{C}_b^{-1} (\boldsymbol{m}-\boldsymbol{m}_b)\right) \tag{10}$$

where N denotes the number of retrieval grid points. The state vector is defined as $\boldsymbol{m} = [u_1, \ldots, u_N, v_1, \ldots, v_N]^{\mathrm{T}}$, while $\boldsymbol{m}_b$ is the corresponding background state). C_b is the covariance matrix of the background wind field.

Under the assumption that the background errors of the u and v components are mutually uncorrelated [43,44], the background-error covariance matrix is explicitly constructed as

$$\boldsymbol{C}_b = \mathrm{diag}\left(\sigma_{b,u}^2 \boldsymbol{I}_N, \sigma_{b,v}^2 \boldsymbol{I}_N\right) \tag{11}$$

where $\sigma_{b,u}$ and $\sigma_{b,v}$ denote the standard deviations characterizing the background errors of the u and v components, respectively, and $\boldsymbol{I}_N$ denotes the $N \times N$ identity matrix.

In principle, background information should be independent of the observational data used in the analysis and is typically provided by model forecasts valid at the analysis time. However, the operational model forecasts often lack the resolution and accuracy required for storm-scale wind field analysis. In fact, the spatial variations of the lidar velocity can provide valuable proxy background for the wind retrieval [45,46], such as the velocity-azimuth display technique [28].

Therefore, the background wind field is obtained by constructing the cost function J, which can be expressed as

$$J = J_b + J_r + J_t \tag{12}$$

$$J_b = \sum_{ij} W_b \left[(u-u_b)^2 + (v-v_b)^2\right] \tag{13}$$

$$J_r = \sum_{i,j} W_r (V_o - V_r)^2 \tag{14}$$

$$J_t = \sum_{i,j} W_t \left(-u \sin\theta + v \cos\theta - \frac{\partial V_o}{\partial \theta} + \frac{\partial u}{\partial \theta} \cos\theta + \frac{\partial v}{\partial \theta} \sin\theta \right)^2 \tag{15}$$

where J_b, J_r, and J_t are the background term, the radial speed term, and the tangential speed term, respectively. u_b and v_b are obtained by minimizing the cost function, when $W_b = 0$. The weighting coefficients are taken as $W_r = 1$ ($m^{-2}s^2$) and $W_t = 0.5$ ($m^{-2}s^2$) [45,46], which are empirically chosen to ensure that the constraints have proper orders of magnitude.

The smoothness prior reflects the underlying physical characteristics of the wind field, namely that the flow should be relatively smooth and consistent with the governing fluid dynamics equations. This constraint is effectively imposed through a zero-mean Gaussian distribution given by

$$p_e(u,v) \propto \exp\left(-\frac{1}{2} \boldsymbol{m}_e^{\mathrm{T}} \boldsymbol{C}_e^{-1} \boldsymbol{m}_e \right) \tag{16}$$

with

$$\boldsymbol{C}_e = \mathrm{diag}\left(\sigma_{\mathrm{div}}^2 \boldsymbol{I}_{N_e}, \sigma_{\mathrm{vor}}^2 \boldsymbol{I}_{N_e}, \sigma_{\mathrm{lap}}^2 \boldsymbol{I}_{N_e} \right) \tag{17}$$

where, σ_{div}, σ_{vor}, and σ_{lap} denote the standard-deviation scales assigned to the divergence, vorticity, and Laplacian, respectively, while $\boldsymbol{I}_{N_e}$ is the $N_e \times N_e$ identity matrix.

The spatial smoothness constraint incorporates the divergence, vorticity, and Laplacian of the retrieved velocity field [47], which can be calculated as

$$\boldsymbol{m}_e = \begin{bmatrix} \boldsymbol{e}_{\mathrm{div}} \\ \boldsymbol{e}_{\mathrm{vor}} \\ \boldsymbol{e}_{\mathrm{lap}} \end{bmatrix} \tag{18}$$

For each grid point ($k = 1, \ldots, N_e$) involved in the spatial smoothness constraints, the divergence, vorticity, and Laplacian residuals are defined as

$$e_{\mathrm{div},k} = \Delta d \left(\frac{\partial u}{\partial x} + \frac{\partial v}{\partial y} \right)_k \tag{19}$$

$$e_{\mathrm{vor},k} = \Delta d \left(\frac{\partial v}{\partial x} - \frac{\partial u}{\partial y} \right)_k \tag{20}$$

$$e_{\mathrm{lap},k} = (\Delta d)^2 \left(\nabla^2 u + \nabla^2 v \right)_k \tag{21}$$

where Δd is the grid size in the retrieval field, and ∇^2 is the Laplacian operator.

These constraints are introduced to ensure that the retrieved horizontal wind field remains spatially plausible and exhibits sufficient smoothness.

2.3.2. Likelihood Function

In the Bayesian inference, a set of measurements y is related to a state vector $\boldsymbol{x}$ (containing parameters describing the atmospheric state) through a forward model $\mathbf{F}$.

$$\mathrm{y} = \mathbf{F}(\boldsymbol{x}, b) + \varepsilon \tag{22}$$

where b is the unretrieved model parameters and ε is the model error. Essentially, the forward model maps the atmospheric state to the corresponding observable variables and contains the physical and instrumental factors associated with the measurement process.

When radial speed measurements from the scanning CDWL at different azimuth angles are used to derive the wind vector components (u, v), the forward model reduces to a geometric relationship that projects the wind vector onto the radial coordinate system. It is given by

$$\mathbf{F} = [\cos\theta, \sin\theta] \tag{23}$$

Since the forward model $\mathbf{F}$ is independent of the state vector $\boldsymbol{x}$, the Jacobian matrix $\mathbf{K}$ with respect to the elements of the state vector $\boldsymbol{x} = [u, v]$ is equal to the forward model itself.

$$\mathbf{K} = \frac{\mathrm{d}\mathbf{F}}{\mathrm{d}\boldsymbol{x}} = \mathbf{F} \tag{24}$$

Eq. (17) can then be linearized as

$$\mathrm{y} = \mathbf{K}\boldsymbol{x} + \varepsilon \tag{25}$$

The likelihood function reflects the difference between the model prediction and the actual observation, which primarily arises from the measurement error of the CDWL system. It is assumed that the measurement errors are independent and follow a zero-mean Gaussian distribution. Therefore, the likelihood function can be expressed as

$$p\left(\sum{}^{o} | u, v \right) = \frac{1}{(2\pi)^{N/2} |\boldsymbol{C}_d|^{1/2}} \exp\left(-\frac{1}{2} (\mathbf{K}\boldsymbol{x} - V_o)^{\mathrm{T}} \boldsymbol{C}_d^{-1} (\mathbf{K}\boldsymbol{x} - V_o) \right) \tag{26}$$

where $\boldsymbol{C}_d$ is the joint covariance matrix.

During the wind field retrieval process, the total measurement error variance σ_ε is used to construct the joint covariance matrix, which is

$$\sigma_\varepsilon^2 = \sigma_r^2 + \sigma_n^2 \tag{27}$$

where σ_r denotes the radial-velocity uncertainty, and σ_n represents the instrumental-noise uncertainty. The former is estimated from the local radial-velocity variability over neighboring range gates, whereas the latter accounts for the signal-quality-dependent measurement precision [27,48].

For a scan with n azimuth angles, the radial velocity uncertainty for the j-th range gate is given by

$$\sigma_r^2(r_j) = \frac{1}{3n} \sum_{i=1}^{n} \sum_{k=j-1}^{j+1} \left(y_r(\theta_i, r_k) - \bar{y}_r(\theta_i, r_j) \right)^2 \tag{28}$$

$$\bar{y}_r(\theta_i, r_j) = \frac{1}{3n} \sum_{k=j-1}^{j+1} y_r(\theta_i, r_k) \tag{29}$$

where n is the total number of azimuth angles. θ_i is the i-th azimuth angle. r_j and r_k denote the j-th and k-th range gates, respectively.

The instrumental-noise uncertainty is selected as 1 m/s according to the signal-to-noise ratio function curve provided [48].

Accordingly, the observation-error covariance matrix is constructed as

$$\boldsymbol{C}_d = \mathrm{diag}\left(\sigma_{\varepsilon,1}^2, \sigma_{\varepsilon,2}^2, \ldots, \sigma_{\varepsilon,N_0}^2 \right) \tag{30}$$

where N_0 denotes the total number of valid radial-velocity observations.

2.3.3. Posterior Probability

The horizontal wind field $\mathbf{L}$ constitutes a high-dimensional vector that typically includes thousands to tens of thousands of unknown parameters (the u and v components at all grid points). The resulting posterior distribution is complex and high-dimensional, making it difficult to integrate or directly sample analytically. The MCMC method can effectively handle this posterior distribution and provide a complete data representation. However, due to the low acceptance rate of traditional MCMC techniques, many sampled values are rejected, resulting in high computational costs.

Gibbs sampling is a special form of the MCMC algorithm that transforms a high-dimensional problem into a one-dimensional problem [49]. Specifically, for the i-th unknown wind velocity component l_i (where l_i can be a u or v component at a grid point), its full conditional

distribution $p(l_i/\mathbf{L}_{-i}, \sum^o)$ depends only on the observed data $\sum^o$ and the current values of all other parameters $\mathbf{L}_{-i}$. The detailed steps of the Gibbs sampling algorithm are as follows [50]:

(1) Initialize sample values of the wind field vector, $\mathbf{L}^0 = \left[l_1^0, l_2^0, \cdots, l_n^0\right]$.
(2) Evolve these samples through t iterations steps to yield $\mathbf{L}^t = \left[l_1^t, l_2^t, \cdots, l_n^t\right]$.
(3) In the $(t+1)$-th iteration, update the sample parameter l_i^{t+1} sequentially based on the following conditional distributions.

$$l_i^{t+1} \sim P\left[l_i \middle| \left(l_1^{t+1}, l_2^{t+1}, \cdots, l_{i-1}^{t+1}, l_{i+1}^t, l_{i+2}^t, \cdots, l_n^t\right), \sum^o\right] \tag{31}$$

where $\left(l_1^{t+1}, l_2^{t+1}, \cdots, l_{i-1}^{t+1}\right)$ is the sample parameter that has been updated in the previous iteration. $\left(l_{i+1}^t, l_{i+2}^t, \cdots, l_n^t\right)$ is the sample parameter that needs to be updated in the current iteration.

For the Gibbs sampler, each retrieval is performed using a chain length of 3000 iterations, with the first 500 iterations discarded as burn-in. Convergence is assessed using four chains with different initial states. The rank-normalized potential scale reduction factor and effective sample size are used as convergence diagnostics, with thresholds of 1.01 and 400, respectively, following [51]. After a sufficient number of iterations, the Markov chain converges to the full posterior distribution. The posterior mean of the Gibbs samples provides the retrieved horizontal wind field, while the standard deviation quantifies the retrieval uncertainty of the retrieval process.

2.4. Evaluation metrics

This paper uses four well-established evaluation metrics to assess the performance of the proposed method in retrieving wind fields. The selected metrics include root mean square error (RMSE), mean absolute percentage error (MAPE), mean absolute error (MAE), and mean bias error (Bias) [52–54]. The principle of the evaluation metrics is that the smaller the RMSE, MAPE, MAE, and Bias values, the better the retrieval performance. The expressions for these metrics are

$$RMSE = \sqrt{\frac{1}{N}\sum_{i=1}^{n}(y_i - \hat{y}_i)^2} \tag{32}$$

$$MAPE = \frac{1}{N}\sum_{i=1}^{N}\left|\frac{y_i - \hat{y}_i}{y_i}\right| \times 100\% \tag{33}$$

$$MAE = \frac{1}{N}\sum_{i=1}^{N}|y_i - \hat{y}_i| \tag{34}$$

$$Bias = \frac{1}{N}\sum_{i=1}^{N}(y_i - \hat{y}_i) \tag{35}$$

where y_i and $\hat{y}_i$ are the observed and predicted value of the wind field, respectively, and N is the number of samples.

3. Experiment and result

3.1. Measurement site and instrumentation

3.1.1. The Ningyang bridge site

The full-scale wind field measurements are conducted at the Ningyang Yangtze River Bridge (NYRB). As shown in Fig. 2, the bridge spans the Yangtze River in a single main span, connecting Yizheng City (Yangzhou) on the north bank to Nanjing and Jurong City (Zhenjiang) on the south bank. The NYRB is a double-tower suspension bridge with a



Fig. 2. Geographical location information of the Ningyang Yangtze River Bridge.

1560 m main span and two side spans measuring 615 m (north) and 552 m (south). The bridge pylons adopt a portal-frame structures, with the north and south towers reaching heights of 248.5 m and 246.5 m, respectively. The main girder is a flat steel box girder designed to carry a six-lane, two-way expressway. This main girder has a total width of 39.1 m and a height of 3.7 m. The terrain surrounding the bridge site is relatively flat and open, with relatively uniform atmospheric turbulence. Owing to its long span and streamlined deck, the NYRB becomes an effective location for studying complex wind-structure interactions.

3.1.2. Long-term instrumentation

The NYRB is equipped with a comprehensive Structural Health Monitoring System (SHMS) to support long-term operational safety assessment. As part of this system, ten ultrasonic anemometers are fixedly installed on the main bridge to monitor the environmental wind loads on the structure, as shown in Fig. 3.

The ultrasonic anemometers provides high-precision measurements, with a wind speed range of 0–60 m/s (accuracy ±1%, resolution 0.01 m/s) and a wind direction range of 0–360° (accuracy ±1°, resolution 0.1°). All anemometers are configured for continuous data acquisition, sampling wind speed and direction at 1 Hz. These anemometers are evenly distributed along the longitudinal axis of the bridge at 390 m intervals to capture wind characteristics at key structural locations. The measurement locations include the tops of the main pylons, the tower-girder junction points, and the quartering points of the main span. This sensor layout provides critical wind information at multiple elevation and span positions of the bridge, which is used to validate the wind field retrieval results based on wind lidar.

3.1.3. Short-term instrumentation

To capture the full-scale spatial structure of the wind field over the river surface, which cannot be resolved by the point-based anemometers, a short-term intensive observation is conducted using a CDWL. Monitoring airflow across the entire 1560 m main span (i.e., distances exceeding 2 km) requires the use of a pulsed Doppler lidar. Continuous-wave lidar systems are unsuitable for this purpose because their probe-length averaging becomes excessive at long ranges, resulting in significant data degradation [55].

As shown in Fig. 4, the CDWL is deployed on the south bank of the river, east of the bridge. This location provided an unobstructed line of sight to the main span and the bridge pylons. During the experiment, the lidar operates primarily in PPI scanning mode to map the horizontal wind field around the bridge deck. Scans are conducted at a low elevation angle of 4.0° to ensure that the beams remain approximately parallel to the river surface and intersect the bridge-girder region. The PPI retrieval grid contains 301 range gates at a radial spacing of 30 m or 15 m, and covers a 70°–120° azimuthal sector at 1° intervals. Since the two horizontal velocity components u and v are retrieved at each grid

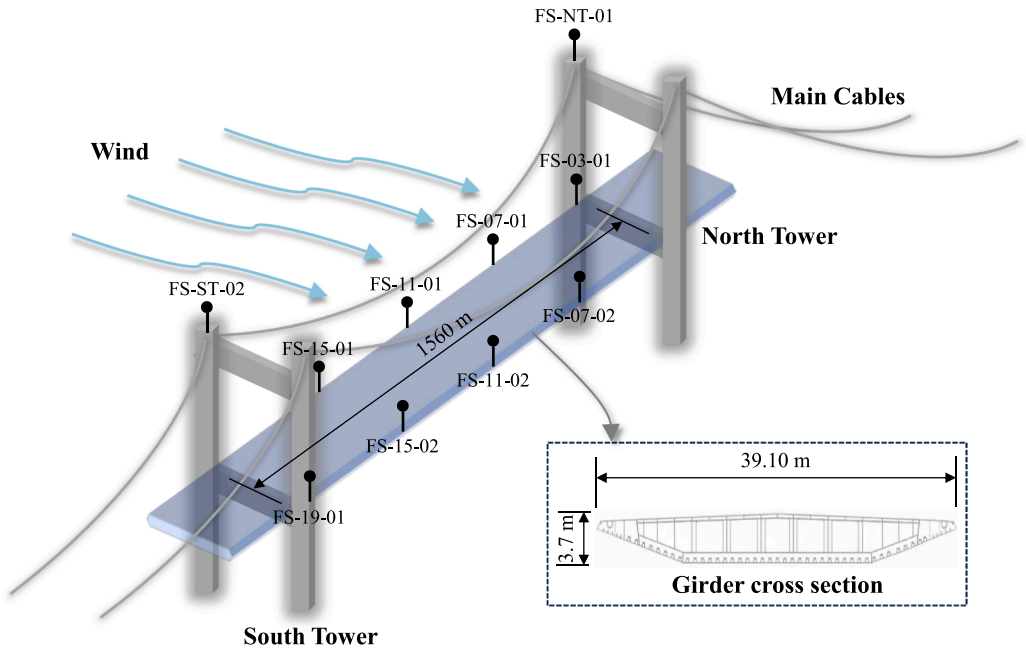


Fig. 3. Schematic diagram of bridge wind field monitoring using ultrasonic anemometers. Hangers are not drawn and the scales are not respected for the sake of clarity.

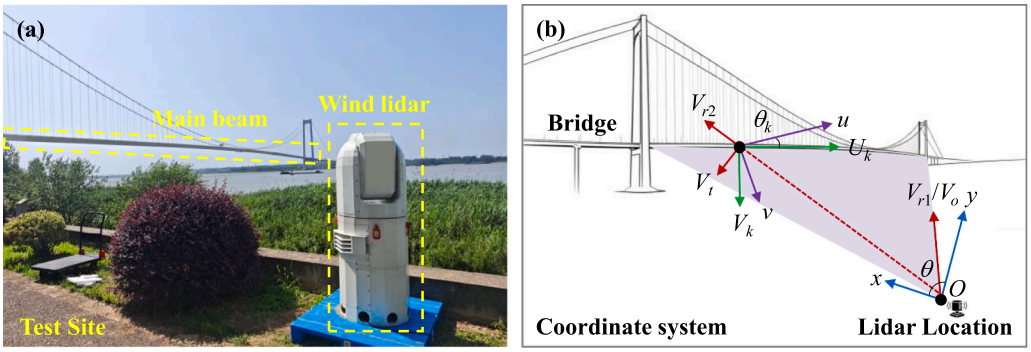


Fig. 4. The on-site wind field observation on the bridge by wind lidar: (a) test site of the wind lidar; and (d) schematic diagram of the coordinate system.

point, the state vector contains up to 72842 unknown velocity components. Each PPI sector scan is completed in approximately 70–120 s, enabling a rapid update of the evolving wind field.

The key technical specifications of the CDWL system are summarized in Table 1. The instrument operates at an eye-safe wavelength of 1.5 μm and provides a maximum detection range of up to 13 km [56]. It offers a high temporal resolution of 0.2–1 s per beam, a configurable spatial resolution (e.g., 15–90 m), and an angular accuracy of 0.01°. The lidar supports multiple scanning patterns, including PPI, range height indicator (RHI), velocity azimuth display (VAD), glide path (GP), and custom defined pattern. The updated CDWL system has undergone extensive optimization, and its reliability has been verified in previous studies [57–59].

Table 1
Key Parameters of the CDWL.

Parameter	Value
Wavelength	1.5 μm
Pulse Energy	300 μJ
Diameter of telescope	80 mm
Repetition frequency	10 kHz
Temporal resolution	0.2–1 s
Spatial resolution	15–90 m
Angle accuracy	0.01°
Maximum range	13 km
Azimuth scanning range	0–360°
Zenith scanning range	0–90°

3.2. Horizontal wind field retrieval

3.2.1. 30 m resolution

To achieve the high CNR long-range scan mode, the pulse width of the CDWL system is initially configured to 200 ns pulse width. The full-scale wind field obtained under this configuration, along with the retrieval results, is presented in Fig. 5. This pulse width typically corresponds to a spatial resolution of 30 m. The primary advantage of this setting is its high pulse energy, which ensures a strong CNR over the long distance covering a main span of 1.56 km.

The radial speed is defined as positive when airflow moves toward the lidar and negative when moving away. The radial wind speed and CNR distributions are shown in Figs. 5(a) and 5(b). Positive radial speeds dominate the lower-left region, whereas negative values occur mainly in the upper-right, indicating a prevailing southwesterly wind. The CNR (red/yellow regions) remains stable within 2 km, confirming the reliability of the long-range signal. Extremely high-CNR regions near [-0.7 km, 1.2 km] correspond to reflections from the main girder and

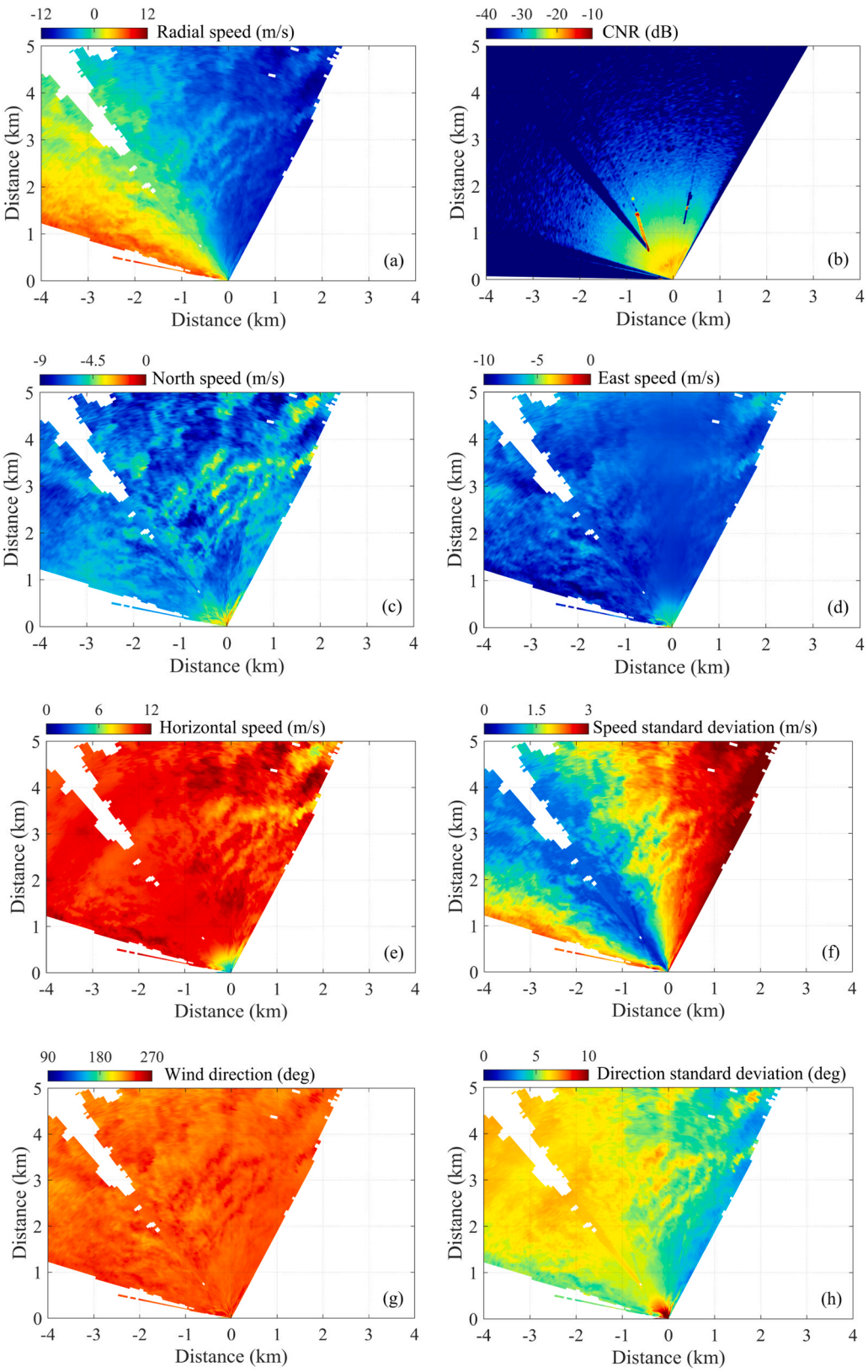


Fig. 5. Wind field and retrieval results at 4.0° and 200 ns: (a) radial speed; (b) CNR; (c) north speed; (d) east speed; (e) horizontal speed; (f) speed standard deviation; (g) horizontal direction; (h) direction standard deviation. The data are recorded from 12:48:00–12:49:59.

provide a reference for the bridge location. Figs. 5(e) and 5(g) present the retrieved horizontal wind speed and direction derived from the north and east wind components. Owing to the complex girder geometry and the low 4.0° scanning angle, ribbon-like velocity disturbances appear around the bridge, characterized by localized velocity fluctuations and directional variations.

The standard deviations of the retrieved wind speed and direction exhibit significant spatial variability, as presented in Figs. 5(f) and 5(h). Wind-speed uncertainty remains low in regions with strong CNR and favorable observation conditions, but increases in the far field as CNR

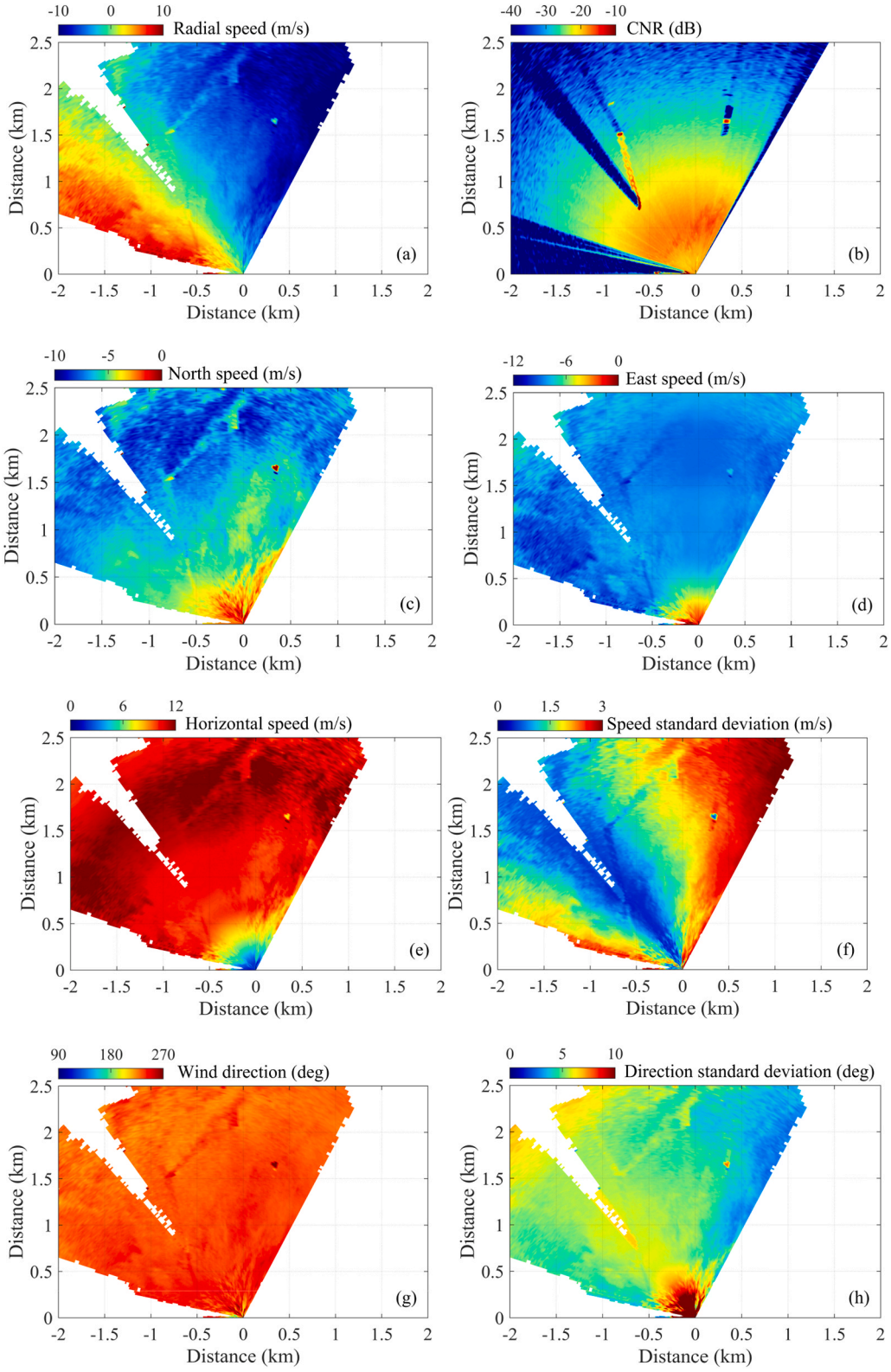


Fig. 6. Wind field and retrieval results at 4.0° and 100 ns: (a) radial speed; (b) CNR; (c) north speed; (d) east speed; (e) horizontal speed; (f) speed standard deviation; (g) horizontal direction; (h) direction standard deviation. The data are recorded from 13:59:21–14:01:21.

decreases, particularly west of the radial-speed "zero line" (approximately 315° azimuth). The directional standard deviation shows a similar pattern, remaining low in the central region and increasing sharply in the far field. In addition, within 0.5 km of the lidar, the limited beam geometry reduces the accuracy of vector retrieval.

As a result, these results validate that the 200 ns configuration effectively captures large-scale, non-uniform turbulent wind fields. The Bayesian framework also successfully retrieves fine-scale flow structures in the horizontal wind field and provides their standard deviations.

3.2.2. 15 m resolution

To fully resolve the wind field at the finest possible scale, CDWL is configured for 100 ns, corresponding to a spatial resolution of 15 m. As the pulse energy decreases and the signal range shrinks, the scanning wind field is geographically focused as a more concentrated sector, with a maximum coverage area of 2.5 km, as shown in Fig. 6.

The raw wind field observation data demonstrate the characteristics of this high-resolution mode, as shown in Figs. 6(a) and 6(b). The CNR decays rapidly, with usable signal becoming weak and noisy beyond 1.5 km. However, this limited range is perfectly sufficient for detailed observation of the bridge site. The high-CNR returns from the main girder clearly identify the focused measurement region, while the radial speed reveals fine-scale flow structures around the bridge. As shown in Figs. 6(c) and 6(d), these features are retained in the retrieved north and east wind components. The 15 m retrieval results exhibit dense, small-scale "ripples", reflecting localized velocity fluctuations.

The retrieved horizontal wind speed and direction further demonstrate the advantages of this configuration, as shown in Figs. 6(e) and 6(g). The "ribbon-like" disturbances observed in the low-resolution scan are resolved into complex clusters of alternating high- and low-speed filaments, together with a distinct shear-layer region downstream of the North Tower. These features are more clearly captured at the 15 m resolution. As shown in Figs. 6(f) and 6(h), the standard deviations of wind speed and direction increase markedly beyond 1.5 km, consistent with the CNR decay and indicating the influence of signal quality on retrieval uncertainty. The Bayesian approach also captures geometry-related uncertainty patterns, including near-field directional instability and the radial-velocity "zero line", further demonstrating its robustness.

Therefore, the 15 m resolution configuration provides a detailed wind field, revealing the fine-scale turbulent and wake structures around the bridge. This results confirms that Bayesian method effectively retrieves the wind field characteristics at this high-fidelity resolution.

3.3. Wind field verification and analysis

3.3.1. Wind speed time-history verification

After analyzing the spatial structure of the horizontal wind field, this section further evaluates the effectiveness of the Bayesian retrieval results using in-situ measurements from multiple ultrasonic anemometers. Due to the obstruction of the main girder, there may be missing wind lidar echo data on the windward side. Therefore, the leeward anemometer has a better spatial correspondence with the wind lidar

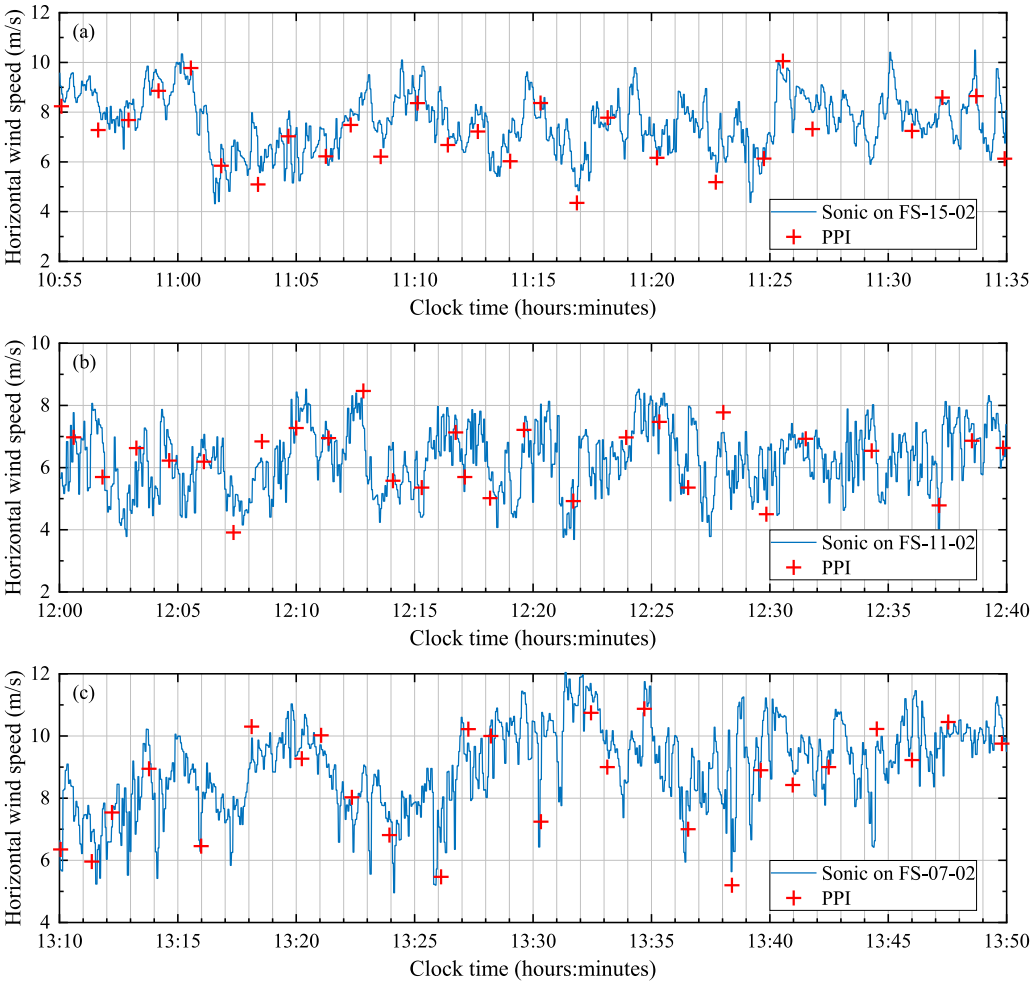


Fig. 7. The time-history curves of wind speed from the anemometer on the bridge and the corresponding lidar-retrieved wind speed results during the period from 10:52–14:42: (a) L/4; (b) L/2; (c) 3 L/4.

retrieval area. The validation results are derived from a relatively long continuous observation period (10:52–14:42) and include three representative locations on the leeward side of the main girder (L/4, L/2, and 3 L/4), as shown in Fig. 7. At midspan, the ultrasonic anemometer is installed 4.0 m above the girder, corresponding to an elevation of 54.1 m. The lidar beam height at midspan is approximately 52.3 m, giving a vertical separation of approximately 1.8 m from the ultrasonic anemometer. The ultrasonic anemometer data used for validation are recorded at 1 Hz. For each PPI scan, the retrieved values at L/4, L/2, and 3 L/4 are paired with the ultrasonic-anemometer observations closest to the corresponding lidar acquisition times, rather than averaged over the complete PPI scanning period.

Although the lidar-derived horizontal wind speed does not resolve the high-frequency peaks observed by the anemometer, it reasonably follows the overall trend of the in-situ measurements. At the L/4 location near the south tower, slight flow disturbances are observed, as shown in Fig. 7(a). Nevertheless, the lidar retrieval captures the gradual increase in wind speed from approximately 7 m/s to 9 m/s between 12:00 and 12:40. At the L/2 location, where the airflow is relatively uniform and minimally disturbed, the retrieved wind speed agrees well with the overall trend of the anemometer measurements, demonstrating good performance of the Bayesian method at mid-span. At the 3 L/4 location, the longer lidar range leads to reduced signal quality, as shown in Fig. 7 (c). Despite the stronger fluctuations recorded by the anemometer, the Bayesian retrieval still captures the temporal evolution of the mean wind speed.

As a result, the wind speed time-history comparison demonstrates that the Bayesian framework successfully and accurately retrieved spatially representative mean airflow at multiple key locations along the bridge deck.

3.3.2. *Influence of prior distributions*

In the Bayesian framework, the prior distribution $p(u,v)$ is crucial for constraining the inherently ill-posed nature of the retrieval problem. The proposed method incorporates two types of priors: the background wind field prior $p_b(u,v)$, which provides valuable initial flow information, and the spatial smoothness prior $p_e(u,v)$ which enforces local smoothness and spatial continuity. To examine the sensitivity of these priors to retrieval accuracy, three models are evaluated:

(1) using only the background prior $p_b(u,v)$.
(2) using only the smoothness prior $p_e(u,v)$.
(3) using the combined prior $p(u,v)$, which integrates both background and smoothness.

The analysis is conducted using 12 consecutive CDWL scans collected between 12:00 and 12:40. For each retrieval, the wind speed and direction at the bridge midspan location are compared with measurements from the supersonic anemometer (FS-11–02), and the total retrieval error is calculated. A detailed quantitative comparison of the wind speed retrieval performance for the three prior distributions is shown in Fig. 8. The four evaluation metrics (RMSE, MAPE, MAE, and Bias) provide a comprehensive assessment of the retrieval accuracy. The results show that relying on a single prior is insufficient.

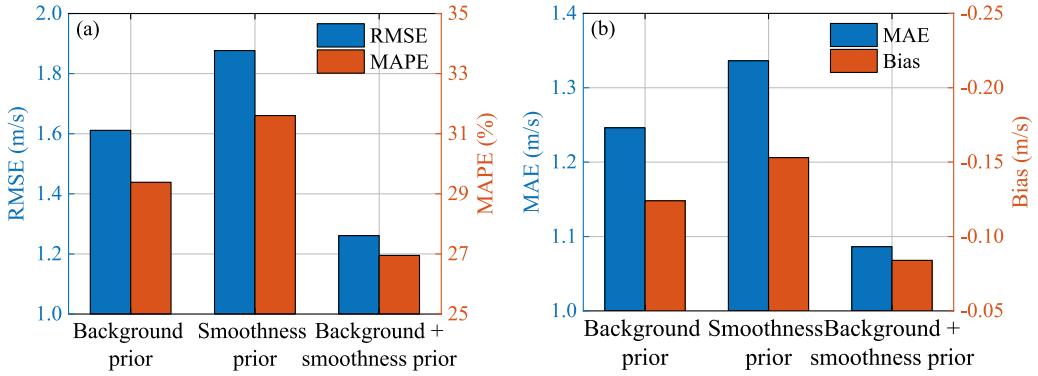
The RMSE and MAPE metrics primarily quantify the overall magnitude of the wind speed retrieval error, as presented in Fig. 8(a). The background prior yields a relatively high RMSE of 1.61 m/s and a MAPE of 29.38%. The background prior yields an RMSE of 1.61 m/s and a MAPE of 29.38%, indicating that it captures the general flow magnitude but still produces notable local errors without smoothness constraints. The smoothness prior performs worse, with an RMSE of 1.87 m/s and a MAPE of 31.60%, showing that the smoothness constraint alone is insufficient without background flow information. In contrast, the retrieval approach that integrates background and smoothness priors demonstrates significant improvements across all evaluation metrics. The RMSE decreases to 1.26 m/s, corresponding to reductions of 21.73% and 32.62% relative to the background and smoothness priors, respectively.

The MAE and Bias metrics primarily characterize the systematic accuracy of the retrieval framework, as shown in Fig. 8(b). The MAE exhibits a similar decreasing trend to RMSE, reflecting a reduction in absolute error. Moreover, the Bias obtained using the combined background and smoothness prior decreases to nearly zero (-0.08 m/s), confirming the improved accuracy and reliability of the retrieved wind field. Therefore, these two priors are complementary and essential for accurate wind speed retrieval.

The wind direction retrieval error exhibits a trend similar to that of the wind speed retrieval error, as shown in Fig. 9. The dramatic influence of the prior distributions on the RMSE of wind direction is presented in Fig. 9(a). The smoothness prior, which lacks background flow information, produces a large RMSE of 8.61°. The background prior performs similarly poorly, yielding an RMSE of 7.45°. In contrast, the combined background and smoothness prior effectively limits the errors, with RMSE reduced by up to 22.18%.

This is further confirmed by examining the MAE and deviation, as shown in Fig. 9(b). The MAE of wind-direction retrieval shows a similar trend. The single-prior cases exhibit relatively large errors, whereas the combined background and smoothness prior achieves the lowest MAE of 5.76°. The single-prior cases also produce larger systematic biases, while the combined prior reduces the Bias to only 0.39°, indicating improved accuracy and reduced systematic deviation in wind-direction retrieval.

These results consistently demonstrate the critical importance of employing a fully informed prior. By integrating both, the combined background and smoothness prior effectively stabilize the retrieval and



(a) RMSE and MAPE (b) MAE and Bias

Fig. 8. Wind speed metric variation for the proposed method under different prior distributions for the anemometer FS-11–02.

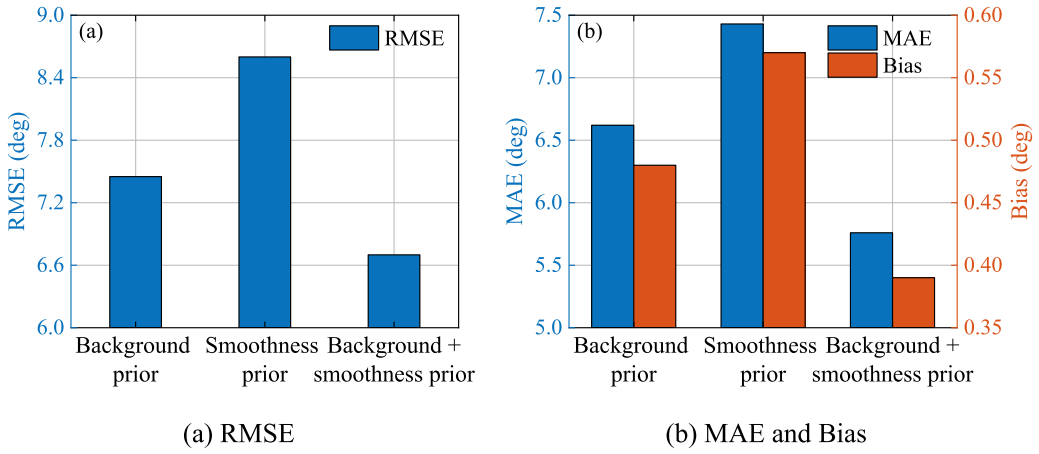


Fig. 9. Wind direction metric variation for the proposed method under different prior distributions for the anemometer FS-11–02.

minimizes errors for wind speed and direction.

3.3.3. *Uncertainty analysis on the main girder*

To validate the reliability of the Bayesian method in quantifying wind field uncertainty, the analysis results at three important locations along the main girder (L/4, L/2, and 3 L/4) are compared with the on-site anemometer measurements. Considering all validation samples from 10:52–14:42 at L/4, L/2, and 3 L/4, 94.2% of the ultrasonic-anemometer wind-speed observations fall within the corresponding 95% confidence interval (CI). The probability density function (PDF) and 95% CI of the retrieved horizontal wind speed at three representative locations are presented in Fig. 10. The red solid line represents the anemometer's measured wind speed, while the red numerical label denotes the corresponding value.

The PDF distribution at the L/4 location near the south tower is relatively broad, as shown in Fig. 10(a). The posterior mean wind speed is 9.78 m/s, while the anemometer records a slightly higher value of 11.87 m/s. The 95% CI range is [6.14, 13.65] m/s, indicating higher uncertainty near the south tower region. In contrast, the PDF at the L/2 location is sharply peaked, with a posterior mean of 10.10 m/s and a narrow CI of [9.03, 11.13] m/s, as illustrated in Fig. 10(b). The anemometer measurement (9.56 m/s) coincides closely with the posterior mean and lies near the center of the CI. This indicate that the uncertainty quantification maintains high accuracy and stability at mid-span, benefiting from a more uniform wind field and high-quality lidar echo signals. At the 3 L/4 location near the north tower, the PDF broadens again, with a posterior mean of 10.24 m/s and a CI of [8.99, 11.45] m/s, as shown in Fig. 10(c). This increased uncertainty is mainly associated with reduced signal quality and stronger downstream flow fluctuations. Overall, the Bayesian method captures the mean wind-

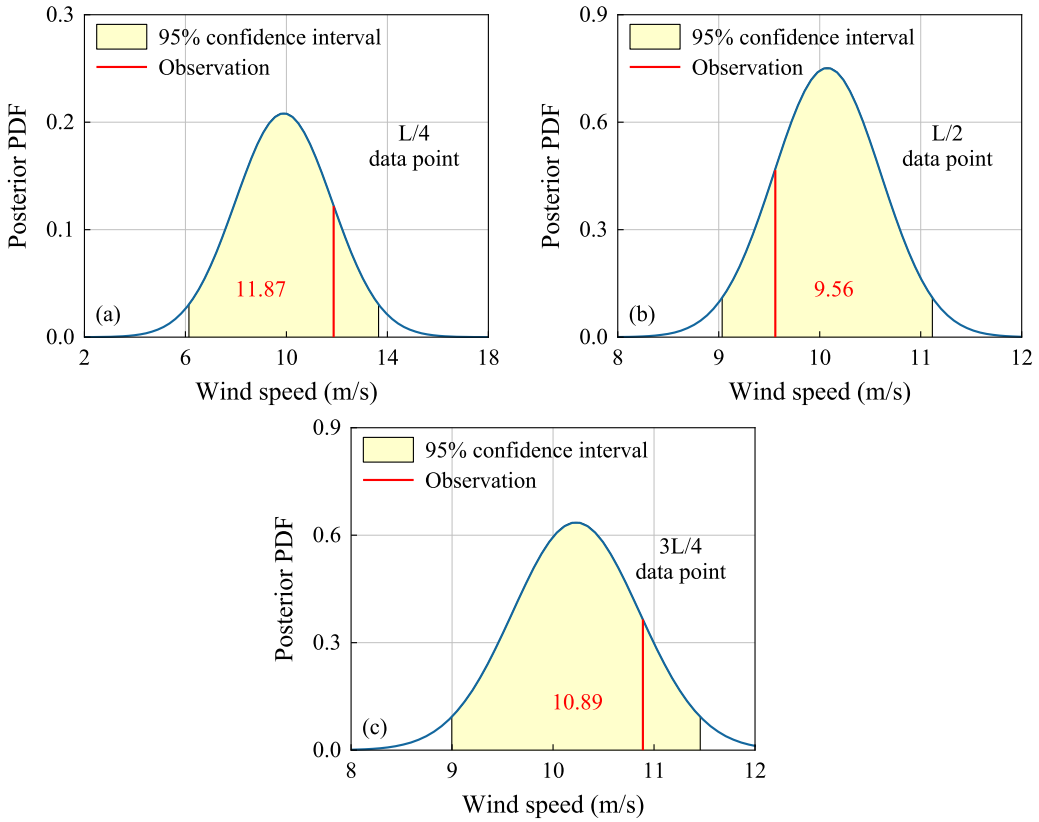


Fig. 10. Three representative cases of PDF and CI of wind speed under 100 ns: (a) L/4; (b) L/2; (c) 3 L/4.

speed variation while quantifying the spatial differences in retrieval uncertainty around the bridge.

For wind direction, 93.6% of the ultrasonic-anemometer observations fall within the corresponding 95% CI over the same validation period and locations. The PDFs and 95% CIs of the retrieved horizontal wind direction at the three key locations along the bridge span (L/4, L/2, and 3 L/4) are presented in Fig. 11. Since wind direction is derived from multiple vector components, it is generally more sensitive to retrieval instability and local flow disturbances.

The posterior PDF at the L/4 location is gradually peaked, with its mean at 243.55°, whereas the anemometer records is 237.15°, as shown in Fig. 11(a). The 95% CI is relatively wide within the range [232.41°, 254.78°], showing a relatively high directional uncertainty. However, the posterior distribution at the L/2 location is narrower and centered at 229.86°, corresponding to a stable westerly flow, as presented in Fig. 11 (b). The 95% CI extends from approximately 219.70° to 239.83°, and the anemometer reading (233.92°) aligns closely with the posterior mean, demonstrating that the Bayesian method achieves high-precision direction retrieval in the mid-span region. The posterior PDF is almost symmetrical at the 3 L/4 location near the north tower, with a mean of 234.61° and a 95% CI of [223.95°, 245.94°], as shown in Fig. 11(c). The anemometer measurement (239.76°) lies close to the upper bound of this high-probability region, suggesting a slight overestimation of wind direction in the retrieved field. This moderate bias and increased uncertainty arise from the wake structure and reduced CNR under the current observation conditions.

These results demonstrate that the Bayesian retrieval framework accurately reproduces the spatially varying mean flow and provides a quantitative characterization of retrieval confidence. The approach thus enables both accurate retrieval of the bridge-scale wind field and quantification of the associated uncertainty required for risk assessment.

3.4. Comparison of different retrieval methods

To comprehensively evaluate the retrieval capability of the proposed Bayesian framework, it is systematically compared with four traditional single-lidar retrieval algorithms using all valid observational data from 10:52–14:42. The selected methods include classical Uniform Wind (UW) [60], Velocity Azimuth Process (VAP) [61], and Velocity Plan Processing (VPP) [62], along with more advanced Variational Method (VM) [45]. A detailed comparison of all evaluation metrics for key locations L/4, L/2, and 3 L/4 is listed in Table 2, including RMSE, MAPE, MAE, and Bias for wind speed and direction.

The comparison of horizontal wind speed errors directly reflects the retrieval performance for the overall mean flow of the wind field. As shown in Table 2, at three locations (L/4, L/2, and 3 L/4), the classical algorithms UW and VAP exhibit the poorest performance, with RMSE ranging from 3.1 to 4.5 m/s. Their high Bias indicates a significant systematic underestimation. This is primarily because these algorithms rely on overly simplistic assumptions (like horizontal homogeneity) that are violated in complex bridge-flow. The VPP method shows moderate improvement, with an RMSE of 2.35 m/s at L/2 location. The VM delivers a substantial enhancement, achieving an RMSE of 1.32 m/s at L/2 location.

On this basis, the proposed Bayesian inference method demonstrates comprehensive and significant superiority, achieving the best performance across all wind speed metrics at the three locations. The method exhibits the lowest RMSE at the favorable L/2 location and maintains similarly low errors at the more complex L/4 and 3 L/4 locations. Specifically, the method achieves an RMSE of 1.15 m/s, representing a 12.87% error reduction relative to the next-best VM and a 51.06% reduction compared with VPP. In addition, the Bias of the method is only −0.07 m/s, which approaches an ideal unbiased state. This superiority arises from the Bayesian framework's ability to integrate smoothness priors with a background prior, allowing it to obtain a more accurate and stable retrieval results than the deterministic method alone.

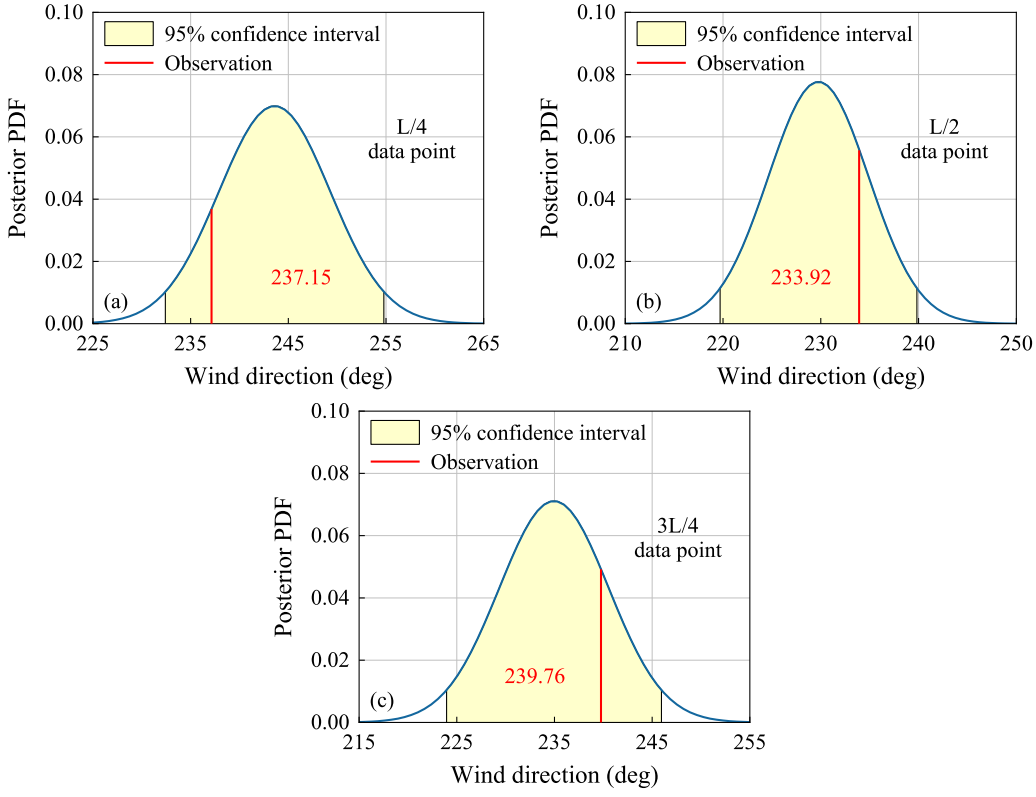


Fig. 11. Three representative examples PDF and CI of wind direction under 100 ns: (a) L/4; (b) L/2; (c) 3 L/4.

Table 2
Performance comparison of different models.

Span	Method	Wind speed				Wind direction		
		RMSE	MAPE	MAE	Bias	RMSE	MAE	Bias
L/4	UW	4.41	0.45	2.08	-0.41	15.28	12.31	-2.62
	VAP	3.25	0.43	1.75	-0.34	14.80	12.56	-1.86
	VPP	2.42	0.38	1.42	-0.23	11.28	8.82	-1.17
	VM	1.58	0.31	1.33	-0.14	8.35	6.77	-0.92
	Bayesian Inference	**1.32**	**0.26**	**1.22**	**-0.09**	**7.42**	**6.20**	**-0.44**
L/2	UW	4.33	0.46	2.04	-0.40	13.86	10.9	-2.34
	VAP	3.18	0.41	1.62	-0.32	11.54	9.38	-1.89
	VPP	2.35	0.35	1.38	-0.21	9.81	7.92	-1.32
	VM	1.32	0.29	1.15	-0.11	7.32	6.03	-0.87
	Bayesian Inference	**1.15**	**0.24**	**1.05**	**-0.07**	**6.10**	**4.82**	**-0.31**
3 L/4	UW	4.52	0.48	2.05	-0.42	14.14	11.43	-2.53
	VAP	3.35	0.40	1.83	-0.35	13.57	11.44	-1.96
	VPP	2.57	0.37	1.57	-0.22	10.45	8.47	-1.34
	VM	1.46	0.30	1.22	-0.12	7.76	6.34	-0.94
	Bayesian Inference	**1.27**	**0.25**	**1.16**	**-0.08**	**6.57**	**5.65**	**-0.38**

Calculating wind direction from different wind vectors presents a challenge to all methods. For wind-direction evaluation, the retrieved directions are expressed in degrees. Wind-direction errors were evaluated using the shortest signed angular difference within [-180°, 180°], thereby accounting for the periodicity of wind direction at the [0°, 360°] boundary. At the 3 L/4 location, the RMSEs of UW, VAP, VPP, and VM are 14.14°, 13.57°, 10.45°, and 7.76°, respectively. The proposed Bayesian method achieves the lowest RMSE of 6.57°, corresponding to improvements of 15.34% over VM and 53.54% over UW. Its Bias at L/4 is also close to zero (0.44°), indicating reduced systematic deviation. These results demonstrate that the Bayesian framework, supported by a posterior distribution, effectively mitigates the ill-posedness of wind direction retrieval.

In summary, the systematic comparison in Table 2 provides clear evidence of the proposed Bayesian method's advantages. Unlike deterministic algorithms, this method achieves the highest wind field retrieval accuracy across the entire bridge span and quantifies the uncertainty associated with the retrieval process. Consequently, the proposed Bayesian inference method establishes a robust foundation for probabilistic wind field Retrieval in complex, large-scale structural environments.

4. Conclusions

This study presents a novel Bayesian inference framework for the retrieval of 2D horizontal wind fields around long-span bridges using CDWL measurements. The proposed approach overcomes the limitations of traditional deterministic algorithms, which provide only single-point estimates. By inferring the full posterior probability distribution of the wind field, the framework enables a rigorous and interpretable quantification of retrieval uncertainty while maintaining high retrieval fidelity. Unlike classical Bayesian methods, the proposed Bayesian retrieval framework integrates background wind field prior and spatial smoothness prior to overcome the inherently ill-posed problem. The framework is validated through full-scale CDWL measurements at the NYRB. Results demonstrate that the combined prior significantly improves the stability and physical consistency of the retrieved wind field compared to a single prior. The anemometer observations on the bridge all fall within the 95% CI range derived from the posterior distribution. In addition, the CI width adaptively adjusts in regions with low CNR or unfavorable lidar geometry, demonstrating the method's ability to propagate uncertainty. The proposed Bayesian framework achieves the highest accuracy and stability when benchmarked against four traditional retrieval algorithms (UW, VAP, VPP, and the VM).

The success of the Bayesian framework highlights the importance of wind lidar to bridge wind engineering, particularly in full-scale bridge wind field measurements. Beyond deterministic estimates, the Bayesian method provides both precision and interpretability, enabling researchers to evaluate wind loading with quantified confidence. Nevertheless, the present validation is based on a single daytime field campaign under a limited range of wind conditions, and broader field observations are still needed to further assess the general applicability of the framework. Future studies can construct independent background fields using high-resolution numerical weather prediction, or independent lidar measurements to evaluate the influence of background-field dependence on posterior uncertainty. Additionally, integrating wind lidar into SHMS may provide a more comprehensive understanding of the bridge-site wind field, thereby supporting wind–bridge interaction analysis and bridge operation management.

CRediT authorship contribution statement

Longwen Fan: Writing – original draft, Visualization, Methodology, Investigation, Formal analysis. **Yiming Zhang:** Writing – review & editing, Supervision, Resources, Funding acquisition, Conceptualization. **Hao Wang:** Writing – review & editing, Supervision, Project administration, Funding acquisition. **Jinlong Yuan:** Writing – review & editing, Visualization, Methodology. **Xiao Pan:** Resources, Data curation. **Shuo Zhang:** Validation, Software. **Haiyun Xia:** Supervision, Resources.

Declaration of Competing Interest

The authors declare that they have no known competing financial interests or personal relationships that could have appeared to influence the work reported in this paper.

Acknowledgements

This work is supported in part by the National Key Research and Development Program of China (No. 2024YFC3014103), the National Natural Science Foundation of China (No. 52338011, 42405137), the Start-up Research Fund of Southeast University (RF1028624058), and the Southeast University Interdisciplinary Research Program for Young Scholars.

Data availability

Data will be made available on request.

References

[1] Chen H, Fang C, Li Y. Nonlinear buffeting responses of a coastal long-span bridge under the coupled wind, wave and current loads. Ocean Eng 2024;293:116661. https://doi.org/10.1016/j.oceaneng.2023.116661.

[2] Hu X, Fang G, Ge Y. Uncertainty propagation of flutter derivatives and structural damping in buffeting fragility analysis of long-span bridges using surrogate models. Struct Saf 2024;106:102410. https://doi.org/10.1016/j.strusafe.2023.102410.
[3] Ma R, Chen N, Ge B, Hu X, Chen A. Probabilistic modeling of wind characteristics for long-span cable-stayed bridges based on field measurements considering deck disturbance effects. Measurement 2023;222:113617. https://doi.org/10.1016/j.measurement.2023.113617.
[4] Zhang J, Jiang F, Zhang M, Zheng H, Li Y, Liang J. Study on joint design method of multiple wind parameters for long-span bridges in deep-cutting gorge areas based on field measurement. J Wind Eng Ind Aerodyn 2024;254:105930. https://doi.org/10.1016/j.jweia.2024.105930.
[5] Chen X, Jiang Y, Zhao N, Jia S, Wang X, Tan S. Simulation of stationary and nonstationary wind velocity field along a long-span bridge using a numerical truncation method. J Wind Eng Ind Aerodyn 2022;231:105206. https://doi.org/10.1016/j.jweia.2022.105206.
[6] Wang H, Li A, Niu J, Zong Z, Li J. Long-term monitoring of wind characteristics at Sutong Bridge site. J Wind Eng Ind Aerodyn 2013;115:39–47. https://doi.org/10.1016/j.jweia.2013.01.006.
[7] Fenerci A, Øiseth O, Rønnquist A. Long-term monitoring of wind field characteristics and dynamic response of a long-span suspension bridge in complex terrain. Eng Struct 2017;147:269–84. https://doi.org/10.1016/j.engstruct.2017.05.070.
[8] Zhang Y, Li H, Wang H. Data-driven wind-induced response prediction for slender civil infrastructure: Progress, challenges and opportunities. Structures 2025;74:108650. https://doi.org/10.1016/j.istruc.2025.108650.
[9] Liu Z, Fang G, Nikitas N, Lan Y, Zhao L, Ge Y. Risk-targeted design wind speeds for multi-level aerodynamic performances of long-span bridges: A real data-informed case study. Struct Saf 2025;117:102637. https://doi.org/10.1016/j.strusafe.2025.102637.
[10] Hu P, Han Y, Cai CS, Cheng W. Wind characteristics and flutter performance of a long-span suspension bridge located in a deep-cutting gorge. Eng Struct 2021;233:111841. https://doi.org/10.1016/j.engstruct.2020.111841.
[11] Sun H, Zhu L-D, Tan Z-X, Zhu Q, Meng X-L. Spanwise layout optimization of aerodynamic countermeasures for multi-mode vortex-induced vibration control on long-span bridges. J Wind Eng Ind Aerodyn 2024;244:105616. https://doi.org/10.1016/j.jweia.2023.105616.
[12] Wang Y, Chen X, Li Y. Nonlinear self-excited forces and aerodynamic damping associated with vortex-induced vibration and flutter of long span bridges. J Wind Eng Ind Aerodyn 2020;204:104207. https://doi.org/10.1016/j.jweia.2020.104207.
[13] Lang T, Wang H, Gao H, Tao T, Xu Z, Gao W. Investigation on vortex-induced vibrations of dual parallel suspenders with different diameters: An enhanced response phenomenon. J Wind Eng Ind Aerodyn 2025;267:106250. https://doi.org/10.1016/j.jweia.2025.106250.
[14] Argentini T, Rocchi D, Somaschini C. Effect of the low-frequency turbulence on the aeroelastic response of a long-span bridge in wind tunnel. J Wind Eng Ind Aerodyn 2020;197:104072. https://doi.org/10.1016/j.jweia.2019.104072.
[15] Zhu L, McCrum D, Sweeney C, Keenahan J. Full-scale computational fluid dynamics study on wind condition of the long-span Queensferry Crossing Bridge. J Civil Struct Health Monit 2023;13:615–32. https://doi.org/10.1007/s13349-022-00657-2.
[16] Chen Q, Yu C, Li Y. Data-driven method for determining the lateral wind profiles loaded on long-span bridges in non-uniform wind fields. Eng Struct 2025;336:120416. https://doi.org/10.1016/j.engstruct.2025.120416.
[17] Ran Y, Chen W-L, Jin Y, Li H, Gao D. Reynolds number sensitivity of the vortex dynamics around a long-span rail-cum-road bridge girder with three separated boxes. J Wind Eng Ind Aerodyn 2024;250:105785. https://doi.org/10.1016/j.jweia.2024.105785.
[18] Li S-M, Xu Y-L, Jiang S-J. Wind field reconstruction and optimal anemometer placement for long span bridges. Adv Struct Eng 2024;27:2823–42. https://doi.org/10.1177/13694332241260868.
[19] Cheynet E, Jakobsen JB, Snæbjörnsson J. Flow distortion recorded by sonic anemometers on a long-span bridge: Towards a better modelling of the dynamic wind load in full-scale. J Sound Vib 2019;450:214–30. https://doi.org/10.1016/j.jsv.2019.03.013.
[20] Wang S, Zhang W, Tian Y, Bao C, Chen Z. Unified numerical model of wind-induced response of long-span structures: Aerostatic torsional divergence, flutter, and random buffeting. Structures 2022;45:1076–94. https://doi.org/10.1016/j.istruc.2022.09.083.
[21] Visich A, Conan B. Measurement and analysis of high altitude wind profiles over the sea in a coastal zone using a scanning doppler LiDAR: Application to offshore wind energy. Ocean Eng 2025;325:120749. https://doi.org/10.1016/j.oceaneng.2025.120749.
[22] Chen A, Yuan J, Yang H, Liu J, Gu Y, Liu Y, et al. Identification and forecasting of low-level wind shear based on long range Doppler wind lidar. Atmos Res 2026;330:108558. https://doi.org/10.1016/j.atmosres.2025.108558.
[23] Nafisifard M, Jakobsen JB, Snæbjörnsson JT, Sjöholm M, Mann J. Lidar measurements of wake around a bridge deck. J Wind Eng Ind Aerodyn 2023;240:105491. https://doi.org/10.1016/j.jweia.2023.105491.
[24] Cheynet E, Jakobsen JB, Snæbjörnsson J, Reuder J, Kumer V, Svardal B. Assessing the potential of a commercial pulsed lidar for wind characterisation at a bridge site. J Wind Eng Ind Aerodyn 2017;161:17–26. https://doi.org/10.1016/j.jweia.2016.12.002.
[25] Chen T, Fu JY, Chan PW, He YC, Liu AM, Zhou W. Wind characteristics in typhoon boundary layer at coastal areas observed via a Lidar profiler. J Wind Eng Ind Aerodyn 2023;232:105253. https://doi.org/10.1016/j.jweia.2022.105253.
[26] Cheynet E, Jakobsen JB, Snæbjörnsson J, Angelou N, Mikkelsen T, Sjöholm M, et al. Full-scale observation of the flow downstream of a suspension bridge deck. J Wind Eng Ind Aerodyn 2017;171:261–72. https://doi.org/10.1016/j.jweia.2017.10.007.
[27] Baidar S, Wagner TJ, Turner DD, Brewer WA. Using optimal estimation to retrieve winds from velocity-azimuth display (VAD) scans by a Doppler lidar. Atmos Meas Tech 2023;16:3715–26. https://doi.org/10.5194/amt-16-3715-2023.
[28] Wildmann N, Päschke E, Roiger A, Mallaun C. Towards improved turbulence estimation with Doppler wind lidar velocity-azimuth display (VAD) scans. Atmos Meas Tech 2020;13:4141–58. https://doi.org/10.5194/amt-13-4141-2020.
[29] Cui L, Ji W, Wei Y. Optimization method for vertical wind velocity retrieval in spaceborne wind field inversion based on the VAD technique. In: Mercorelli P, Jiang Z, Wang C, editors. Second International Conference on Remote Sensing Technology and Survey Mapping (RSTSM 2025). Beijing, China: SPIE; 2025. p. 22. https://doi.org/10.1117/12.3067806.
[30] Kelberlau F, Mann J. Better turbulence spectra from velocity–azimuth display scanning wind lidar. Atmos Meas Tech 2019;12:1871–88. https://doi.org/10.5194/amt-12-1871-2019.
[31] Shapiro A, Robinson P, Wurman J, Gao J. Single-Doppler Velocity Retrieval with Rapid-Scan Radar Data. J Atmos Ocean Technol 2003;20:1758–75. https://doi.org/10.1175/1520-0426(2003)020<1758:SVRWRR>2.0.CO;2.
[32] Zhao Y, Yuan L, Fan C, Zhu X, Liu J, Dai B, et al. Wind retrieval for genetic algorithm-based coherent Doppler wind lidar employing airborne platform. Appl Phys B 2023;129:36. https://doi.org/10.1007/s00340-023-07984-2.
[33] Nabney IT, Cornford D, Williams CKI. Bayesian inference for wind field retrieval. Neurocomputing 2000;30:3–11. https://doi.org/10.1016/S0925-2312(99)00136-8.
[34] Albani RAS, Albani VVL, Gomes LES, Migon HS, Silva Neto AJ. Bayesian inference and wind field statistical modeling applied to multiple source estimation. Environ Pollut 2023;321:121061. https://doi.org/10.1016/j.envpol.2023.121061.
[35] Yan Y, Zhang Y, Zhou L, Zhang F, Wang H. Acoustic signals-based probabilistic fault diagnosis for expansion joints of small and medium bridges using Bayesian ensemble learning. Eng Struct 2026;354:122379. https://doi.org/10.1016/j.engstruct.2026.122379.
[36] Valikhani M, Jahangiri V, Ebrahimian H, Moaveni B, Liberatore S, Hines E. Inverse modeling of wind turbine drivetrain from numerical data using Bayesian inference. Renew Sustain Energy Rev 2023;171:113007. https://doi.org/10.1016/j.rser.2022.113007.
[37] Stoffelen A, Portabella M. On Bayesian scatterometer wind inversion. IEEE Trans Geosci Remote Sens 2006;44:1523–33. https://doi.org/10.1109/TGRS.2005.862502.
[38] Adamo M, Rana FM, De Carolis G, Pasquariello G. Assessing the Bayesian inversion technique of C-band synthetic aperture radar data for the retrieval of wind fields in marine coastal areas. J Appl Remote Sens 2014;8:083531. https://doi.org/10.1117/1.JRS.8.083531.
[39] Zhang Y-M, Wang H, Mao J-X, Xu Z-D, Zhang Y-F. Probabilistic Framework with Bayesian Optimization for Predicting Typhoon-Induced Dynamic Responses of a Long-Span Bridge. J Struct Eng 2021;147:04020297. https://doi.org/10.1061/(ASCE)ST.1943-541X.0002881.
[40] Wang H, Zhang Y-M, Mao J-X. Sparse Gaussian process regression for multi-step ahead forecasting of wind gusts combining numerical weather predictions and on-site measurements. J Wind Eng Ind Aerodyn 2022;220:104873. https://doi.org/10.1016/j.jweia.2021.104873.
[41] Dempster AP. A Generalization of Bayesian Inference. J R Stat Soc Ser B Stat Methodol 1968;30:205–32. https://doi.org/10.1111/j.2517-6161.1968.tb00722.x.
[42] Williams CKI, Rasmussen CE. Gaussian Processes for Regression. Adv Neural Inf Process Syst 1995;8.
[43] Fukuda J, Barbot S. Ensemble Kalman inversion for spatially varying rheological parameters in a stress-driven model of post-seismic deformation. Geophys J Int 2025;242:ggaf208. https://doi.org/10.1093/gji/ggaf208.
[44] Romero J, Heidrich W, Ravasi M. Bayesian seismic inversion with implicit neural representations. Geophys J Int 2025;242:ggaf249. https://doi.org/10.1093/gji/ggaf249.
[45] Qiu C-J, Shao A-M, Liu S, Xu Q. A two-step variational method for three-dimensional wind retrieval from single Doppler radar. Meteorol Atmos Phys 2006;91:1–8. https://doi.org/10.1007/s00703-004-0093-8.
[46] Chan PW, Shao AM. Depiction of complex airflow near Hong Kong International Airport using a Doppler LIDAR with a two-dimensional wind retrieval technique. Metz 2007;16:491–504. https://doi.org/10.1127/0941-2948/2007/0220.
[47] Yuan J, Su L, Xia H, Li Y, Zhang M, Zhen G, et al. Microburst, Windshear, Gust Front, and Vortex Detection in Mega Airport Using a Single Coherent Doppler Wind Lidar. Remote Sens 2022;14:1626. https://doi.org/10.3390/rs14071626.
[48] Newsom RK, Brewer WA, Wilczak JM, Wolfe DE, Oncley SP, Lundquist JK. Validating precision estimates in horizontal wind measurements from a Doppler lidar. Atmos Meas Tech 2017;10:1229–40. https://doi.org/10.5194/amt-10-1229-2017.
[49] Geyer CJ. Practical Markov Chain Monte Carlo. Stat Sci 1992;7:473–83.
[50] Ching J, Muto M, Beck JL. Structural Model Updating and Health Monitoring with Incomplete Modal Data Using Gibbs Sampler. Comp-Aided Civil Eng 2006;21:242–57. https://doi.org/10.1111/j.1467-8667.2006.00432.x.
[51] Vehtari A, Gelman A, Simpson D, Carpenter B, Bürkner P-C. Rank-Normalization, Folding, and Localization: An Improved R̂ for Assessing Convergence of MCMC (with Discussion). Bayesian Anal 2021;16. https://doi.org/10.1214/20-BA1221.

[52] Hodson TO. Root-mean-square error (RMSE) or mean absolute error (MAE): when to use them or not. Geosci Model Dev 2022;15:5481–7. https://doi.org/10.5194/gmd-15-5481-2022.
[53] Chicco D, Warrens MJ, Jurman G. The coefficient of determination R-squared is more informative than SMAPE, MAE, MAPE, MSE and RMSE in regression analysis evaluation. PeerJ Comput Sci 2021;7:e623. https://doi.org/10.7717/peerj-cs.623.
[54] Cawley GC, Talbot NLC. On Over-fitting in Model Selection and Subsequent Selection Bias in Performance Evaluation. J Mach Learn Res 2010;11:2079–107.
[55] Mikkelsen T, Mann J, Courtney M, Sjöholm M. Windscanner: 3-D wind and turbulence measurements from three steerable doppler lidars. IOP Conf Ser Earth Environ Sci 2008;1:012018. https://doi.org/10.1088/1755-1315/1/1/012018.
[56] Wang C, Xia H, Shangguan M, Wu Y, Wang L, Zhao L, et al. 1.5 μm polarization coherent lidar incorporating time-division multiplexing. Opt Express 2017;25:20663. https://doi.org/10.1364/OE.25.020663.
[57] Yuan J, Xia H, Wei T, Wang L, Yue B, Wu Y. Identifying cloud, precipitation, windshear, and turbulence by deep analysis of the power spectrum of coherent Doppler wind lidar. Opt Express 2020;28:37406–18. https://doi.org/10.1364/OE.412809.
[58] Wang L, Qiang W, Xia H, Wei T, Yuan J, Jiang P. Robust Solution for Boundary Layer Height Detections with Coherent Doppler Wind Lidar. Adv Atmos Sci 2021;38:1920–8. https://doi.org/10.1007/s00376-021-1068-0.
[59] Jia M, Yuan J, Wang C, Xia H, Wu Y, Zhao L, et al. Long-lived high-frequency gravity waves in the atmospheric boundary layer: observations and simulations. Atmos Chem Phys 2019;19:15431–46. https://doi.org/10.5194/acp-19-15431-2019.
[60] Persson P.O.G., Andersson T. Automatic wind field interpretation of Doppler radar radial wind components. 1987.
[61] Liang X. An Integrating Velocity–Azimuth Process Single-Doppler Radar Wind Retrieval Method. J Atmos Ocean Technol 2007;24:658–65. https://doi.org/10.1175/JTECH2047.1.
[62] Lang X, Wei M, Ge W, Dang R. A new method of retrieving wind field using single Doppler radar. Sci Meteor Sin 2001;21:417–24.